Impacts of extreme events on hydrodynamic characteristics of a submerged floating tunnel

P.X. Zou [a,b,c,*], Jeremy D. Bricker [a,d], Wim S.J. Uijttewaal [a]

[a] *Delft University of Technology, 2600GA, Delft, the Netherlands*
[b] *CCCC FHDI Engineering Co., Ltd., Guangzhou Guangdong, 510230, China*
[c] *CCCC SFT Technical Joint Research Team, Zhuhai Guangdong, 519080, China*
[d] *Dept. of Civil and Environmental Engineering, University of Michigan, Ann Arbor, MI, 48109, USA*

A B S T R A C T

A submerged floating tunnel (SFT) is a promising alternative to conventional bridges and tunnels, and can be potentially built in the Qiongzhou Strait in China. However, this area is under the threat of disasters including mega tsunamis and severe storm surges. To evaluate the hydrodynamic loads of the SFT in this hazardous zone subject to severe tsunami and typhoon impacts, the Delft3D-FLOW hydrodynamic model and SWAN wave model are coupled, and a Computational Fluid Dynamics (CFD) method is adopted. The maximum probable tsunami and typhoon Rammasun (July 2014) are selected as hazard assessment conditions in the Qiongzhou Strait. Whether the tsunami and hindcast storm surge cause extreme forcing and bring challenges to the SFT engineering design, operation, and maintenance in the Qiongzhou Strait are discussed in this study. We reveal that the typhoon impacts are more devastating than tsunami for an SFT in the Qiongzhou Strait. In order to determine the optimal SFT cross-section under extreme events, we use a parametric Bezier curve profile compared with two simpler shapes including circular and elliptical cross sections. In-line force and lift are respectively applied to evaluate the SFT's hydrodynamic behaviour. Our results reveal that the gross horizontal force on the parametric Bezier curve shape is more sensitive to flow acceleration, while the circular cross-section is dominated by current speed. The parametric Bezier curve cross-section shape has the preferable property of reducing the in-line force and postponing serious vortex shedding compared with the two simpler shapes.

1. Introduction

The Submerged Floating Tunnel (SFT) is a novel sea-crossing infrastructure moored afloat from the seafloor, with the advantage of shortened travel distance, increased environmental adaptability, and reduced construction cost compared with traditional alternatives such as immersed tunnels, bored tunnels, and bridges (Fig. 1). A potential SFT construction site, the Qiongzhou Strait (Fig. 2), located between Hainan Island and Leizhou Peninsula (Guangdong) in the South China Sea (SCS), is subject to extreme events (Zhang et al., 2010)– (Jiang et al., 2018). The SFT is at risk of damage due to current and wave actions, internal flooding and submergence. Extreme hydraulic events further exacerbate the structural vulnerability.

The Qiongzhou Strait is located approximately 1000 km away from the Manila Trench, and is conceivably threatened by a Manila Trench tsunami. The Manila Trench and the north fault system are identified as being the most likely sources to generate mega submarine earthquake-tsunamis in the SCS and adjacent areas (Michel et al., 2001). Research about earthquake-tsunami generation along the Manila Trench has been conducted over the past two decades. Wu and Huang (2009) generated a hypothetical tsunami scenario from the Manila Trench and performed tsunami run-up and inundation simulations around Taiwan. Liu et al. (2009) discussed the characteristics of tsunamis generated by earthquakes along the Manila subduction zone and proposed an early warning system for the SCS region. Hong Nguyen et al. (2014) assessed the impact of a Manila Trench tsunami on the Vietnamese coast using the COMCOT model. Zhao et al. (2017) discussed a range of potential tsunami source magnitudes in the Manila Trench and analysed the tsunami impacts near Haikou. Ren et al. (2017) investigated the potential extreme hazard of the Manila Trench, and the impacts on Hainan Island, Taiwan Island, and Lingding Bay. As one of the most devastating natural coastal disasters, tsunamis frequently occur and caused
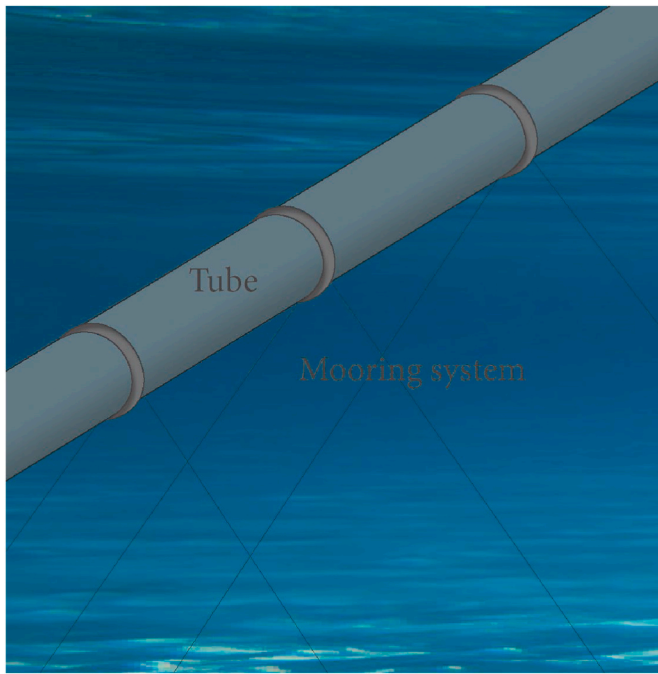
Fig. 1. Schematic configuration of an SFT system.

Fig. 2. Typhoon Rammasun track.

approximately 250,000 casualties and US$280 billion in economic losses during the past twenty years. Devastating tsunami damages, characterized by human fatalities and infrastructure failures, have increased over the previous two decades (Imamura et al., 2019), (Bernard and Titov, 2015). Thus, assessing large-scale tsunami impact in the Qiongzhou Strait is important for hazard mitigation, and tsunami warning capacity improvement is needed for intensive growth of infrastructure and critical engineering facilities such as an SFT in this region.

Storm surges are also catastrophic natural disasters for marine and coastal zones. Storm surge is an abnormal sea level rise driven by physical mechanisms including the inverse barometer (pressure) effect setup, wind-induced setup and breaking-wave setup (BRICKERet al., 2014). The Northwest Pacific basin holds the highest tropical storm surge frequency and intensity occurrence in the world with approximately 26.9 events annually. Guangdong and Hainan, where the Qiongzhou Strait is located, are particularly vulnerable to catastrophic

typhoon strikes (biu Liu et al., 2001). Moreover, the frequency of tropical storm surges and coastal floods in the coastal areas of China over the past 65 years has risen significantly. Amongst the coastal provinces, Guangdong suffered the most storm surge events, while Hainan ranked fourth for storm surge frequency (Shi et al., 2015). The losses caused by storm surges accounted for over 75% of total economic losses, an annual average of more than CNY 3.9 billion in these tropical coastal provinces (Shi et al., 2015). However, little is known about the effects of cross-oceanic tsunami and typhoon-related strait hydrodynamics on the SFT. Risk and vulnerability assessment due to tsunami and typhoon hazards on an SFT in this region had not yet been conducted.

In this study, the worst-case tsunami scenario along the Manila Trench and super typhoon Rammasun (2014) are selected as the extreme scenarios. To better understand hydrodynamic performance of the SFT under the tsunami and storm surge, we ask (1) how to determine the typical wave and current input conditions for the SFT analysis under these extreme cases, (2) which SFT cross-section shape is favourable and should be adopted for locations subject to extreme events, and (3) what is the effect of storm surge and tsunami on an SFT? To address these questions, first, descriptions of the selected scenarios and potential SFT application sites are depicted in section 2, and the modelling methods are then expanded in section 3. In section 4, tsunami and storm surge model validations are conducted. Finally, the wave and current characteristics induced by extreme events at the optimal SFT construction location in the Qiongzhou Strait are addressed in section 5, along with detailed discussions about the optimal SFT cross-section geometry and hydrodynamic characteristics.

2. Description of selected extreme events and analysis location

2.1. Tsunami generated in the Manila Trench

The largest historical tsunamigenic earthquake in the Manila Trench (Wu and Huang, 2009) was simulated as six fault segments acting as one long earthquake source in this study. The worst-case Manila Trench source parameters used in our model are proposed by Hong Nguyen et al. (2014), which modifies Wu and Huang (2009)'s model with more precise fault width values by an interpolation method (Megawatiet al., 2009). Table 1 shows the hypothetical fault parameters along the Manila Trench source applied in this study, with epicenters set at the midpoint of each segment. The earthquake magnitude is 9.3.

2.2. Typhoon Rammasun

As the most powerful and strongest typhoon to make landfall on Hainan Island since 1949, super typhoon Rammasun (2014) is selected as an extreme event for hydrodynamic assessment of the SFT. Rammasun made first landfall on Wenchang, Hainan at 7:00 UTC on July 18, 2014 with a maximum wind speed of 60 m/s and a minimum pressure of 910 hPa. After that, Rammasun retained super typhoon intensity while crossing the Qiongzhou Strait and moving north-westward. It weakened when it entered Beibu Gulf, and dissipated when it made its second landfall in Guangxi province on July 19. Rammasun is the most devastating typhoon that affected Hainan Island since 1949. It affected 3.26 million people, collapsed 23,160 residences, and caused direct economic losses of CNY 11.95 billion in Hainan (Haikou Meteorological Service, 2020). The track (Fig. 2) and intensity data are obtained from the China Meteorological Administration tropical cyclone database (CAM Tropical Cyclone Data).

2.3. Optimal submerged floating tunnel heading

Yan et al. (2016) and Shengzhong et al. (2016) compared seven possible sea-crossing locations in the Qiongzhou Strait, considering submarine geomorphological features, structure reliability, and economy. "*Line V*" (from Sitang in Leizhou Peninsula to Tianwei in Haikou),

Table 1
Fault parameters of the manila trench.

Fault	Long.	Lat.	Length (km)	Width (km)	Dislocation (m)	Depth (km)	Strike (°)	Dip (°)	Rake (°)
E1	120.5	20.2	190	120	25	30	354	10	90
E2	119.8	18.7	250	160	40	30	22	20	90
E3	119.3	17	220	160	40	30	2	28	90
E4	119.2	15.1	170	90	28	30	356	20	90
E5	119.6	13.7	140	110	12	30	344	22	90
E6	120.5	12.9	95	80	5	30	331	26	90

shown in Fig. 3, was recommended as the optimal SFT construction heading. It is selected for SFT hydrodynamic analysis under the tsunami and storm surge impacts in this study. Seven virtual gauges are set uniformly along this optimal heading to obtain the hydrodynamic conditions in the strait during the simulated events. The coordinate of each virtual gauge is listed in Table 2.

3. Methodology

3.1. Model description

The numerical hydrodynamic modelling system Delft3D-FLOW is applied to perform both the tsunami and storm surge simulations. It solves the unsteady, non-linear shallow water equations. Delft3D-FLOW is a widely-used prediction tool for tsunami events, tidal flows and wind-pressure fields (Yin et al., 2020; Roeber and Bricker, 2015; Bricker and Nakayama, 2014). For tsunami simulation, the seafloor deformation of a tsunami-generating earthquake can be computed by the Okada model derived from a Green's function solution to the elastic half space problem (Okada, 1992). The static deformation of the seafloor after the oceanic earthquake is then estimated as an initial free-surface profile. The initial water level of the Manila Trench tsunami is shown in Fig. 4.

The behaviour of typhoon Rammasun is hindcast with track data (CAM Tropical Cyclone Data) spatialized into wind and pressure fields by the Holland (Holland et al., 2010) parametric hurricane method, which improves the Holland (1980) parametric approach by applying wind-pressure parameters readily available from hurricane archives. Empirical relations for central pressure and maximum wind speed are devised by Holland (2008). The wind field is asymmetric due to the inflow angle caused by friction. Here, a constant angle of 25° is applied (Wankang et al., 2019). A wind conversion factor of 0.93 is adopted. The radius of maximum winds R_m is expressed per Gross et al. (2004) in Eq. (1)

$$R_m = 35.37 - 0.111V_m + 0.570(\phi - 25) \tag{1}$$

Table 2
Coordinates of virtual gauges.

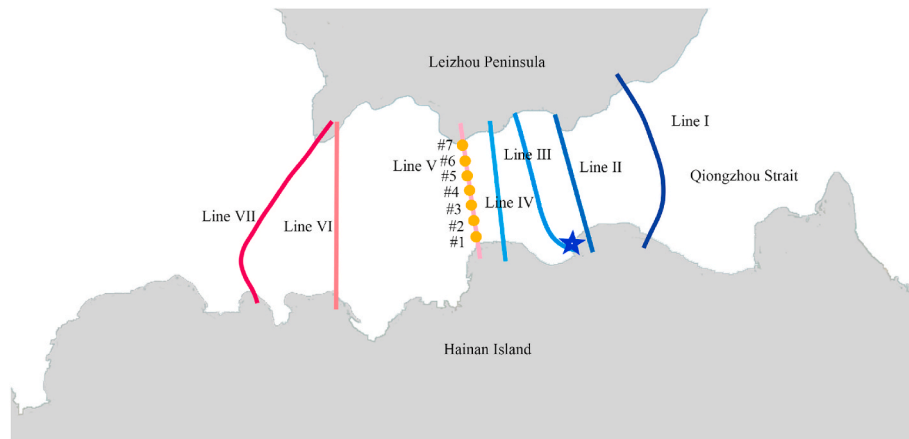|	Latitude (°N)	Longitude (°E)
Gauge #1	20.084	110.168
Gauge #2	20.108	110.166
Gauge #3	20.132	110.164
Gauge #4	20.156	110.162
Gauge #5	20.180	110.160
Gauge #6	20.204	110.158
Gauge #7	20.252	110.154

where V_m is the maximum wind speed and ϕ is latitude.

An integrated atmosphere-ocean storm surge modelling framework is established for SFT hydrodynamic forcing evaluation. The typhoon Rammasun wind-pressure fields drive a Delft3D-FLOW hydrodynamic model and SWAN wave model. In order to account for wave-current interaction and radiation stresses, online coupling of SWAN with Delft3D-FLOW is activated. The air-sea drag coefficient is 0.003, and a Manning's n of 0.025 sm$^{-1/3}$ is used for bottom stress. Open boundaries use a water level prescribed by the Global Inverse Tide Model TPXO 7.2 (OSU TPXO Tide Model, 2020) (M2, S2, N2, K2, K1,O1, P1, Q1, MF, MM, SSA components) with the "*pavbnd*" command to prevent instability when interacting with meteorological forcing (Caldwell and Edmonds, 2014). The bathymetry data is taken from the General Bathymetric Chart of the Oceans (GEBCO, 2020).

In this study, large-scale tsunami and typhoon models are established respectively to analyze depth-averaged flow characteristics in the Qiongzhou Strait. The in-line component of the current and wave loads at planes perpendicular to the optimal SFT heading line ("*Line V*") are emphasized in the evaluation of the SFT cross-section forcing.

3.2. Model configuration

The geographic extent of the model domain ranges from 105°E, 26°N

Fig. 3. The seven alternative headings for sea-crossing in the Qiongzhou Strait and the virtual gauge locations (yellow circles) along "*Line V*". The blue star denotes the observation station at Xiuying (110.34°E, 20.05°N) used for model validation. (For interpretation of the references to colour in this figure legend, the reader is referred to the Web version of this article.)
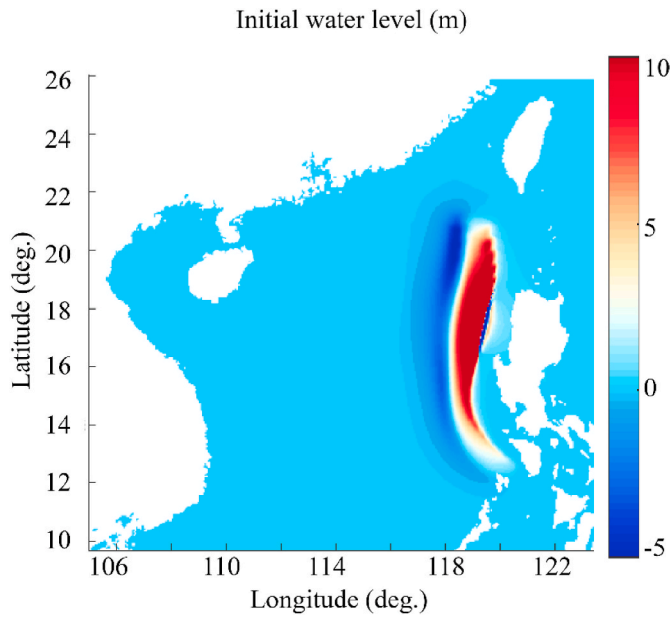
Initial water level (m)

Fig. 4. Initial water level profile along Manila Trench.

to 126°E, 10°N. Three nested grids, referred to as Grid 1, Grid 2, and Grid 3, are adopted with spherical coordinates. The finest grid covers the Qiongzhou Strait to obtain the flow and wave conditions (Fig. 5). Detailed grid information is shown in Table 3. A 0.5 s computational time step for a duration of 12 h is applied in the tsunami simulation. In the storm surge simulation, a 1 s computational time step is selected for the storm surge model, which is coupled with a stationary SWAN wave simulation every 60 min. Wind-stress and tidal forcing are added to run the simulation from 0:00 on July 14 to 0:00 on July 20.

3.3. Cross-section geometry

Most SFT cross-sections have been designed with a circular shape (Lin et al., 2019; Jin and Kim, 2020; Deng et al., 2020), primarily due to the superior hydrodynamic and blast load behaviour compared with a rectangular shape (Gang et al., 2018), (Kristoffersen et al., 2019). An elliptical cross-section has more streamlined hydrodynamic behaviour, experiencing smaller displacement and less stress than circular and
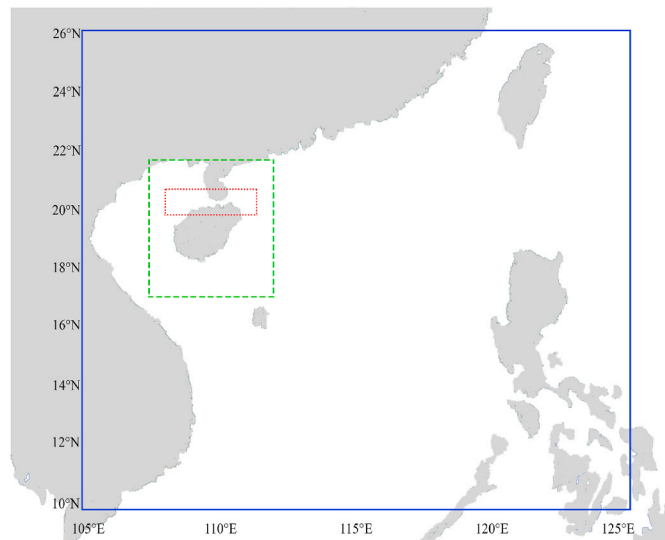

Fig. 5. Computational domain and nested grids.

Table 3
Three-level grid parameters.

Level	Grid 1	Grid 2	Grid 3
Grid resolution (degree)	0.05	0.01	0.002
Central Point	115.5°E, 18°N	110.2°E, 19.7°N	110.2°E, 20.15°N
Number of cells in longitude direction	420	520	2200
Number of cells in latitude direction	320	580	350

rectangular shapes (Li and Jiang, 2016), (Mandara et al., 2016). However, in this study, in order to minimize the transverse force and continuously improve the streamlined shape, we use an airfoil geometry parameterization method based on the Bézier-PARSEC (BP) curve to describe the SFT cross-section, combining the merits of the Bézier curve with PARSEC variables (Chen et al., 2019; Christie et al., 2019; Derksen and Rogalsky, 2010). In order to determine the optimal SFT cross-section, the hydrodynamic performance of this parametric Bézier curve profile is tested and compared with the simpler circular and elliptical shapes under the tsunami impact. The detailed parametric Bézier curve information (the definitions of b, y_t, r) is described in (Kharal and Saleem, 2012), (Zou et al., 2020). In this study, we choose the Bezier parameters $b = 1.5$ m, $r = 0.5$ m, and $y_t = 4$ m to design the SFT cross-section. As per the current technical standards and feasibility studies (Muhammad et al., 2017), (AASHTO, 2018), the cross-section must provide sufficient space for traffic, evacuation, ventilation, ballast, inspection and other services and utilities. In order to fix the shape parameters for comparison, SFT cross-sections with lateral and vertical clearances of $H = 5$ m and $W = 11$ m, respectively (as required by road tunnel construction guidelines), is selected for the hydrodynamic analysis of all the three shapes (Fig. 6). The semi-minor axis of elliptical shape is 4 m, to keep the same vertical clearance as the parametric Bezier curve SFT profile.

3.4. Forces on the submerged floating tunnel

The CFD code ANSYS FLUENT v19.1 is applied to conduct field-scale simulations of the SFT by solving the RANS equations using a finite-volume discretization scheme. Considering the different hydrodynamic performance of the SFT under tsunami and typhoon impacts, the computational domain is different for each case.

3.4.1. Governing equations

The tsunami affects the SFT by generating strong currents. Strong acceleration of these currents causes the SFT boundary layer to alternate between laminar and turbulent flow, and inertial forces on the SFT are significant. To resolve these processes, a transient simulation is conducted with the transition SST (shear stress transport) turbulence model, which has been validated to accurately predict the laminar to turbulent transition process (Langtry and Menter, 2009). Previous studies show the reliability of this turbulence model at both low and high Reynolds numbers (Wauters and Degroote, 2018; Pawar and Brizzolara, 2019; Xu et al., 2018).

The transition SST model is based on coupling of the SST k-ω transport equations with the intermittency and momentum-thickness Reynolds number transport equations for the transition onset criterion. The intermittency factor used to describe transition development is computed by additional transport equations in the form of Eq. (2)

$$\begin{cases} \dfrac{\partial}{\partial t}(\rho\gamma) + \dfrac{\partial}{\partial x_j}(\rho\gamma U_j) = \dfrac{\partial}{\partial x_j}\left[\left(\mu + \dfrac{\mu_t}{\sigma_\gamma}\right)\dfrac{\partial\gamma}{\partial x_j}\right] + P_{\gamma1} - E_{\gamma1} + P_{\gamma2} - E_{\gamma2} \\[2ex] \dfrac{\partial}{\partial t}\left(\rho\widetilde{Re_{\theta t}}\right) + \dfrac{\partial}{\partial x_j}\left(\rho\widetilde{Re_{\theta t}}U_j\right) = \dfrac{\partial}{\partial x_j}\left[\sigma_{\theta t}(\mu + \mu_t)\dfrac{\partial\widetilde{Re_{\theta t}}}{\partial x_j}\right] + P_{\theta t} \end{cases}$$
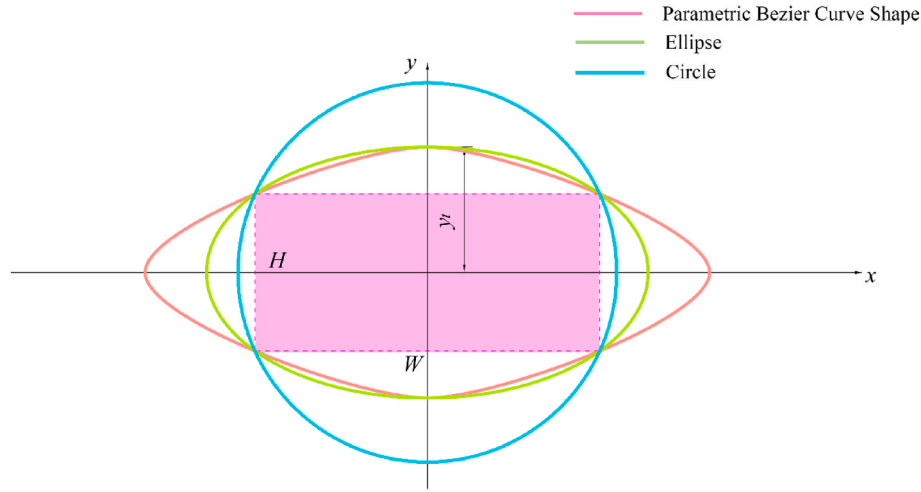
(2)

Fig. 6. Three SFT cross-sections dimension sketch.

where $\sigma_\gamma = 1.0$, $\sigma_{\theta t} = 2.0$. $P_{\gamma 1}$, $E_{\gamma 1}$ are transition sources, $P_{\gamma 2}$, $E_{\gamma 2}$ are destruction or relaminarization sources; $P_{\theta t}$ is a source term; $\widetilde{Re_{\theta t}}$ is the transition momentum thickness Reynolds number; U is upstream flow velocity; γ is intermittency; μ is viscosity; μ_t is eddy viscosity; and ρ is fluid density. Detailed formulations of the transition SST model are given in reference (Coder and Maughmer, 2013).

For the storm surge case, however, strong flow acceleration is not observed in the Qiongzhou Strait as per section 5.2. Hence, the inertial force of the SFT can be neglected. In order to achieve a conservative hydrodynamic force evaluation for the SFT, a worst-case scenario of the maximum current velocity and wave height is applied at the numerical inlet. The Reynolds number of the SFT cross-section is on the order of 10^7. Therefore, a fully-turbulent model can be used. The RNG k-ε model is applied at high Reynolds numbers, and is more accurate and reliable for a wider class of flows than the standard k-ε model (Jeong et al., 2002). It more accurately simulates blunt geometry and flow separation with an additional term in the ε equation and an analytical formula for the turbulent Prandtl number. The RNG k-ε model transport equation can be expressed as Eq. (3)

$$\mu_t = \rho C_\mu \frac{k^2}{\varepsilon} \tag{5}$$

where $C_\mu = 0.085$.

The volume-of-fluid (VOF) method (Hirt and Nichols, 1981) is adopted to track the air-water interface. This method is accomplished by the solution of a continuity equation for the volume fraction σ of the ith phase. The volume fraction equation is obtained with Eq. (6), and the fluid viscosity μ and density ρ in each grid cell are reconstructed by volume phase averaging with Eq. (7)~(8):

$$\frac{\partial \sigma_i}{\partial t} + \nabla \cdot (\sigma_i \vec{v_i}) = 0 \tag{6}$$

$$\rho = \sum_{i=1}^{n} \sigma_i \rho_i \tag{7}$$

$$\mu = \sum_{i=1}^{n} \sigma_i \mu_i \tag{8}$$

$$\begin{cases} \dfrac{\partial}{\partial t}(\rho k) + \dfrac{\partial}{\partial x_i}(\rho k u_i) = \dfrac{\partial}{\partial x_j}\left(\alpha_k \mu_{eff} \dfrac{\partial k}{\partial x_j}\right) + G_k + G_b - \rho\varepsilon - Y_M + S_k \\[3mm] \dfrac{\partial}{\partial t}(\rho\varepsilon) + \dfrac{\partial}{\partial x_i}(\rho\varepsilon u_i) = \dfrac{\partial}{\partial x_j}\left(\alpha_\varepsilon \mu_{eff} \dfrac{\partial \varepsilon}{\partial x_j}\right) + C_{1\varepsilon}\dfrac{\varepsilon}{k}(G_k + C_{3\varepsilon}G_b) - C_{2\varepsilon}\rho\dfrac{\varepsilon^2}{k} + G_b - R_\varepsilon + S_\varepsilon \end{cases} \tag{3}$$

where $C_{1\varepsilon} = 1.42$ and $C_{2\varepsilon} = 1.68$ are dimensionless user-adjustable parameters derived using the RNG theory. μ_{eff} is effective viscosity; k is turbulence kinetic energy; ε is turbulence dissipation rate; G_k and G_b are generation terms; Y_m is the contribution of the fluctuating dilatation of compressible turbulence to the overall dissipation rate; α_k and α_ε are inverse effective Prandtl numbers; S_k and S_ε are source terms. The additional term in the ε equation is given by Eq. (4)

$$R_\varepsilon = \frac{C_\mu \rho \eta^3 (1 - \eta/\eta_0)}{1 + \beta\eta^3} \frac{\varepsilon^2}{k} \tag{4}$$

where, $\eta \equiv S_k/\varepsilon$, $\eta_0 = 4.38$, and $\beta = 0.012$. The turbulent viscosity is computed by combining k and ε as Eq. (5)

where σ is the volume fraction of the ith phase, and v_i is the velocity of the ith phase.

Fifth-order Stokes wave theory (Fenton, 1985) is used for nonlinear wave generation at the inlet open channel wave boundary. The generalized expression for fifth-order Stokes waves is given by Eqs. (9) and (10)

$$\zeta(X, t) = \frac{1}{k} \sum_{i=1}^{5} \sum_{j=1}^{i} b_{ij} \left(\frac{kH}{2}\right)^i \cos(j\alpha) \tag{9}$$

$$\alpha = k_x x + k_y y - \omega_e t + \varepsilon \tag{10}$$

The generalized expression for the associated velocity potential is defined as Eq. (11)

$$\Phi(X,t) = \frac{1}{k}\left(\frac{g}{k}\tanh(kh)\right)^{\frac{1}{2}}\sum_{i=1}^{5}\left(\frac{kH}{2}\right)^{i}\sum_{j=1}^{i}a_{ij}\cosh[jk(z+h)]\cos(j\alpha) \tag{11}$$

Velocity components for surface gravity waves are shown in Eq. (12)

$$\begin{cases} u = \dfrac{\partial \Phi}{\partial x}\cos\theta \\[2mm] v = \dfrac{\partial \Phi}{\partial x}\sin\theta \end{cases} \tag{12}$$

The wave frequency ω is given by Eq. (13)

$$\omega = [gk\tanh(kh)]^{\frac{1}{2}}\left[1 + c_3\left(\frac{kH}{2}\right)^2 + c_5\left(\frac{kH}{2}\right)^4\right] \tag{13}$$

where ω_e is effective wave frequency; t is time; k is wave number; h is water depth; g is the gravity magnitude; a_{ij}, b_{ij}, c_i are the complex expressions of kh; H is wave height; θ is the wave heading angle.

3.4.2. Computational domains

For the tsunami, a time series of flow speed during the 12 h tsunami simulation period is applied at the inlet boundary. A transient analysis with a symmetrical (in the vertical) computational domain is adopted. The computational domain is 400 m in length and 100 m in height (Fig. 7(a)). The distances from the inlet and outlet boundaries to the SFT cross-section center are 100 m and 300 m, respectively. A zero-reference pressure and zero-gradient condition for velocity are employed at the pressure-outlet boundary. A no-slip, hydraulically smooth wall condition is applied to the SFT cross-section surface. For the upper and lower boundaries, symmetry (free-slip) is used to avoid wall effects. Multiple grid sizes were used to evaluate grid independence in (Zou et al., 2020). The computational domain comprises three regions as illustrated in Fig. 7 (a). The first region: a high-quality unstructured mesh is generated
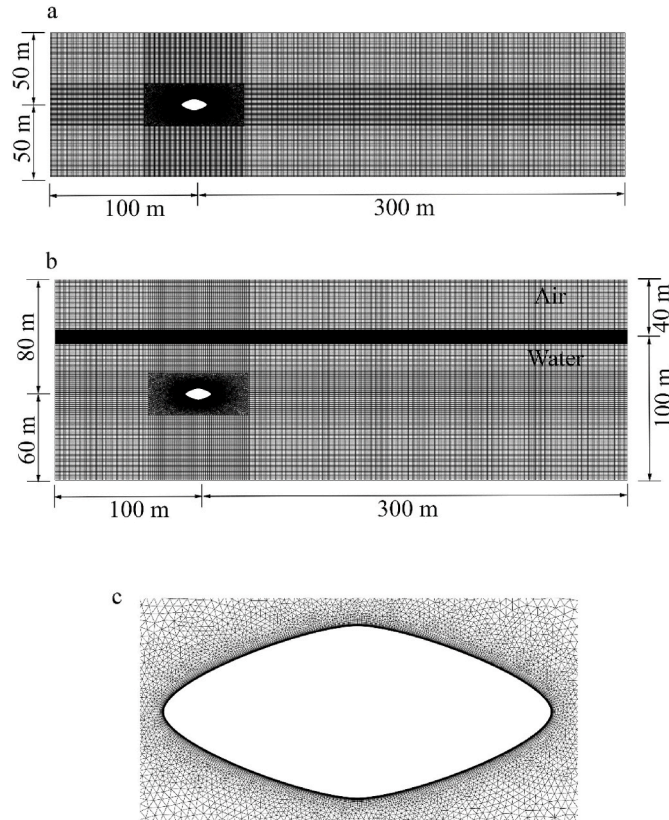

Fig. 7. Schematic of meshes used. (a) Computational domain for tsunami simulation. (b) Computational domain for storm surge simulation. (c) Detailed mesh around the SFT.
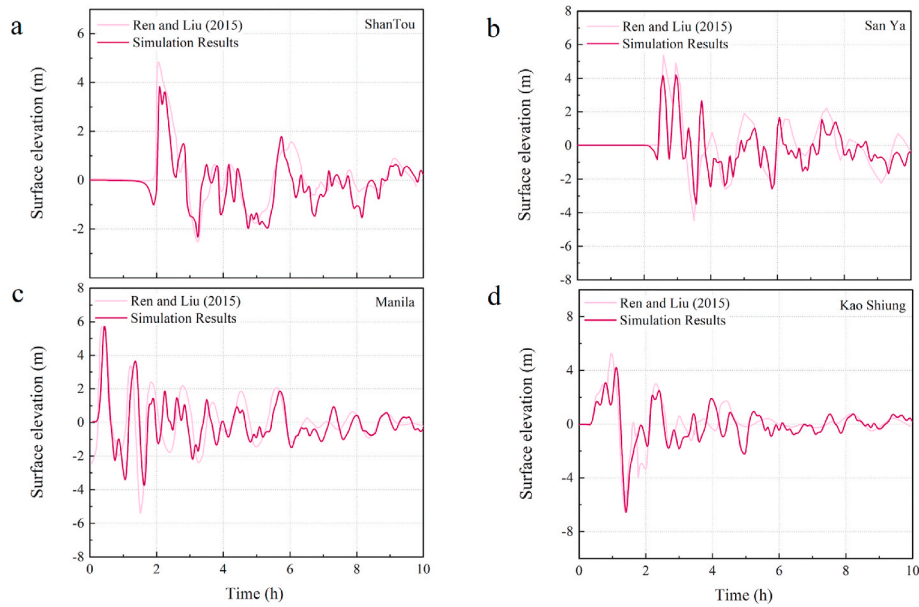
around the SFT cross-section, and an inflation tool is used to generate 40 layers of quadrangular cells covering the boundary layer of the SFT surface. The first grid layer cell size normal to the SFT cross-section surface is 3×10^{-5} m with a growth rate of 1.2, resulting in y + around 1 (Fig. 7(c)). The cell size parallel to the surface is 0.01 m. The second region: the 4 zones around the first region have a grid resolution of 0.5 m. The third region: a structured mesh with a grid resolution of 1 m is applied in the rest of the domain. The total number of cells in this model is about 300,000. The PISO (Pressure-Implicit with Splitting of Operators) algorithm is used for pressure-velocity coupling. The CFD simulation runs for the full tsunami generation and propagation process of 12 h. A high-performance computing (HPC) cluster is used to run parallel computation tasks.

Since wind-induced wave effects need to be considered in the storm surge case, a numerical open channel wave flume is established. The computational domain is 400 m in length and 140 m in height, allowing 9 wavelengths to propagate in the numerical flume (Fig. 7(b)). The water depth is 100 m based on the topography of the optimal SFT heading in the Qiongzhou Strait. The height of the air phase is 40 m. The SFT is submerged at a depth of generally 30–50 m below the free surface as per the feasibility studies and relevant research to date with the consideration of reducing surface wave impacts and meeting navigation requirements (il Seo et al., 2015), (Kunisu, 2010). Herein, an SFT submergence depth of 40 m is adopted. From section 5.2, the maximum current acceleration is below 8×10^{-5} m/s² during the storm surge simulation, indicating the inertial force (due to storm-surge-induced current) acting on the SFT can be neglected. In order to simulate the most unfavorable condition, a combined steady current and wave condition is applied. From the results of section 5.2, an open channel wave boundary condition with wave height $H = 4.8$ m and wave length $L = 45$ m, coupled with a mean current speed of 1.65 m/s are specified at the inlet boundary. 5th order Stokes wave theory with an Ursell number of 0.0097 is applied to depict the wave profile. The wave and current propagate in the same direction (left to right). Zero-reference pressure is employed at the open channel pressure outlet and the top boundary in the air region to avoid back flow into the domain. A hydraulically smooth no-slip wall condition is applied on the SFT cross-section surface and at the bottom boundary. The grid is almost the same as tsunami case except for two differences: 1) Since the Reynolds number in the storm surge study is higher than the tsunami case, and each case uses a different turbulence model, in order to meet the required y+, the first grid layer length normal to the SFT cross-section surface is 1×10^{-3} m. 2) A fine grid near the free surface and higher order discretization are applied to reduce numerical dissipation of waves. The grid resolution near the free surface covers 100 nodes per wave height and 45 nodes per wave length. This local refinement sufficiently captures the wave profile as per previous studies (Tian et al., 2019), (Li and Zhang, 2019). The total number of cells in this model is 473,252 after mesh refinement. A 400s simulation is performed, and the last 100s of data, in which the force oscillation is stable, is used for force analysis.
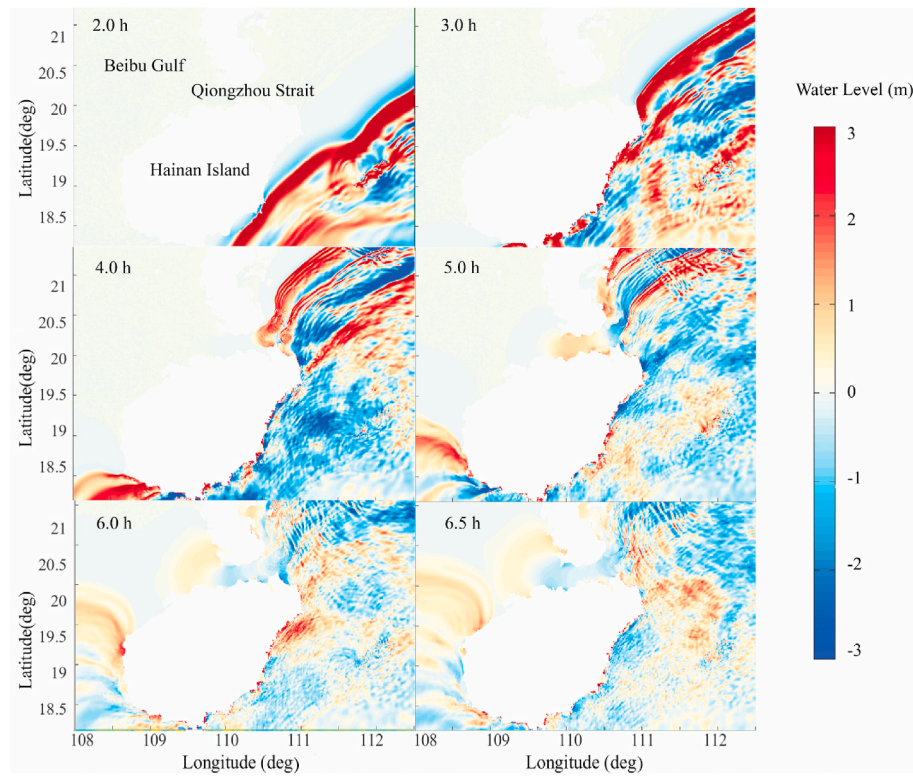
4. Model validation

4.1. Tsunami case

Modelled surface elevations at several locations from Ren et al. (2017) are used to validate our results. Fig. 8 shows our simulated tsunami surface levels and phases are in close agreement with Ren et al. (2017)'s model in general. Mesh precision differences and steep topography near the coastal regions may cause slight deviation of the peak values at Sanya, KaoShiung, and Shantou. Fig. 9 shows the tsunami propagation at several times near the Qiongzhou Strait. The tsunami wave first hits the south-eastern shore of Hainan Island at around 2 h, and thereafter refracts around Hainan Island into two separate parts: one propagates from north-eastern Hainan Island into the Qiongzhou Strait, and another bypasses south-western Hainan Island into the Beibu Gulf.

Fig. 8. Time series of water levels at different locations. (a)~(d): temporal variation of surface elevation at Shantou, San Ya, Manila, and Kao Shiung, respectively.

Fig. 9. Tsunami propagation near the Qiongzhou Strait at different times.

The onset of tsunami waves in the Qiongzhou Strait appears at 4 h, and the confluence of the two waves occurs at 6.5 h near north-western Hainan Island. The arrival time and temporal variation of tsunami amplitude around the Qiongzhou Strait agree with Ren et al. (2017), indicating the robustness and reliability of our results.
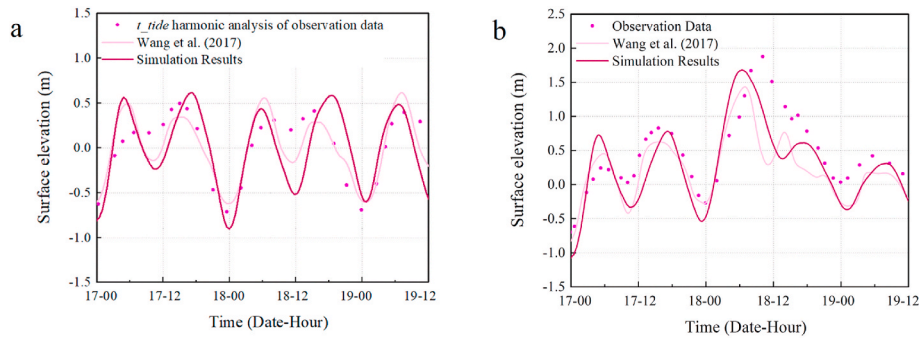
4.2. Typhoon case

In order to verify our results, two simulations are carried out. One contains only astronomical tidal forcing, and the other is comprised of tidal forcing plus the meteorological forcing from the typhoon to compute the total storm tide elevations. Here, during typhoon Rammasun, the measured data of tidal station Xiuying (Fig. 3), which is located in the Qiongzhou Strait, is utilised to validate model results. The model results of Wang et al. (2017) are also used for comparison.

Fig. 10 (a) shows the validation results for astronomic tides at Xiuying (110.34°E, 20.05°N). Even though the simulated results show a positive bias of 16 cm at the maximum surface elevation, the astronomical tides are generally consistent with Wang et al. (2017)'s model results and *t_tide* harmonic analysis. The storm tide elevation during

Fig. 10. Time series of water levels at different locations. (a) Astronomical tide validation. (b) Storm tide validation. The water elevation is referenced to Mean Sea Level.

typhoon Rammasun in Xiuying is shown in Fig. 10 (b). Typhoon Rammasun crossed over the Qiongzhou Strait during high tide. The maximum water elevation (storm tide) is almost 2 m above mean sea level. The peak storm tide is underestimated by 20 cm in our model, whereas Wang et al. (2017)'s model underestimated observed data by approximately 40 cm. Both our model and (Wang et al., 2017) predicted the highest storm tide about 3 h earlier than observed. Since the best track data for the storm is reported at 6 h intervals, the meteorological input data cannot be expected to produce a result more accurate than this, as the storm location and propagation speed is not constant during the 6 h between reported track times. Therefore, our results show less discrepancy with observations than (Wang et al., 2017) does, indicating a reasonable and reliable storm surge simulation and confirming the capacity of the model.

5. Results and discussion

5.1. Tsunami characteristics in the Qiongzhou Strait

To investigate the tsunami characteristics in the Qiongzhou Strait, the maximum water elevation at each grid cell during the entire 12 h simulation is shown in Fig. 11(a). Generally, water elevations decrease

Fig. 11. Hydraulic properties of the Manila Trench tsunami in the Qiongzhou Strait. (a) Maximum water surface elevation. (b) Maximum east-west current magnitude.

from the east at around 2 m to the west at less than 1 m in the Qiongzhou Strait. Throughout the simulation, our results show that the Qiongzhou Strait is sheltered by Hainan Island, preventing the devastating inundation that could occur in Hainan, Guangdong, Taiwan, and Hong Kong (Wu and Huang, 2009; Ren et al., 2017).
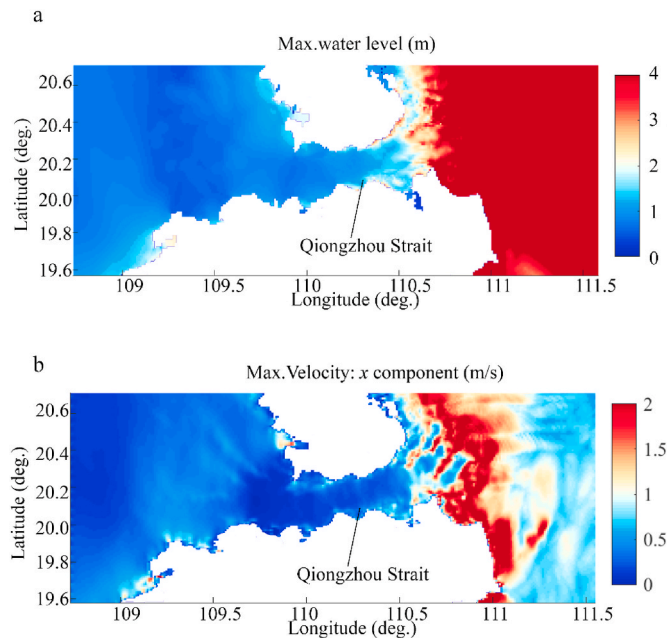
Since the optimal SFT heading is generally transverse to the strait, the components of current speed and wave direction parallel to the strait heading are most relevant for evaluation of the SFT cross-section hydraulic performance. Fig. 11 (b) shows the maximum east-west current speed induced by the tsunami in the Qiongzhou Strait. In most of the Qiongzhou Strait, the current speed is less than 1 m/s. The current direction is generally east-west, moving between the Beibu Gulf and the northern SCS. Since the tsunami is unsteady, the time-varying current speed and inflow acceleration may change dramatically, and hence may cause large drag and inertial forces on the SFT compared with the local astronomical tide, jeopardizing the SFT structure and mooring system. To assess the effect of this east-west reversing tsunami current on the SFT, the current in the Qiongzhou Strait is extracted for the simulation of forces on the SFT.

Fig. 12 (a) shows the depth-averaged along-strait current speed at the seven gauges (Fig.(3)) in the Qiongzhou Strait during the tsunami simulation. Note that it takes 4.2 h for the first tsunami wave to arrive at the SFT site. The first current peak occurs at 4.8 h, with a maximum speed of 0.6 m/s in the westward direction. However, the largest current speed occurs at around 11.3 h, flowing from west to east with a maximum speed of 0.9 m/s. Generally, gauge #7 records the most severe current speed variation, so is used for further SFT hydrodynamic analysis. Fig. 12 (b) shows the current speed and flow acceleration at gauge #7. It should be noted that the peak values of flow speed and acceleration do not occur simultaneously. The largest flow acceleration magnitude is 6×10^{-4} m/s^2 in the westward direction at 4.5 h.

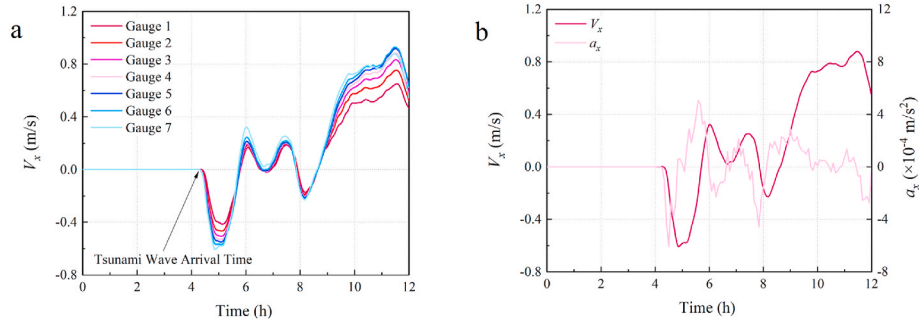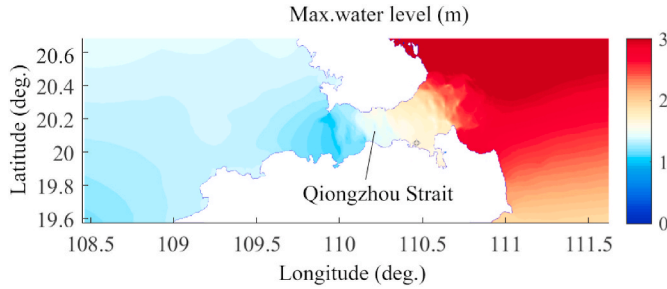### 5.2. Storm surge characteristics in the Qiongzhou Strait

Fig. 13 shows the spatial distribution of maximum water level (storm tide) in the Qiongzhou Strait during the typhoon simulation. Typhoon Rammasun passed over north eastern Hainan Island with a counterclockwise wind field. These effects were conductive to the sea water rising rapidly to the east of the Qiongzhou Strait and piling up along the coasts, especially near the Leizhou Peninsula and northeastern Hainan Island. The maximum water level on the eastern coast of the Leizhou Peninsula reached over 3 m. However, due to the sheltering effect of the Leizhou Peninsula and Hainan Island, and additionally the gradually weakened strength of Rammasun when it crossed over the Qiongzhou Strait, the maximum water elevation in the strait was less than 2 m, dropping rapidly to the west.

The current speed and wave direction transverse to the SFT are extracted for hydraulic performance analysis. As illustrated in Fig. 14 (a), the maximum absolute value of depth-averaged flow speed observed in gauge #3 in the x direction is 1.65 m/s westward. The peak value

Fig. 12. Tsunami characteristics in the Qiongzhou Strait. (a) Current speed at the seven virtual gauges. (b) Current speed and acceleration at virtual gauge #7. x direction: positive eastward and negative westward.
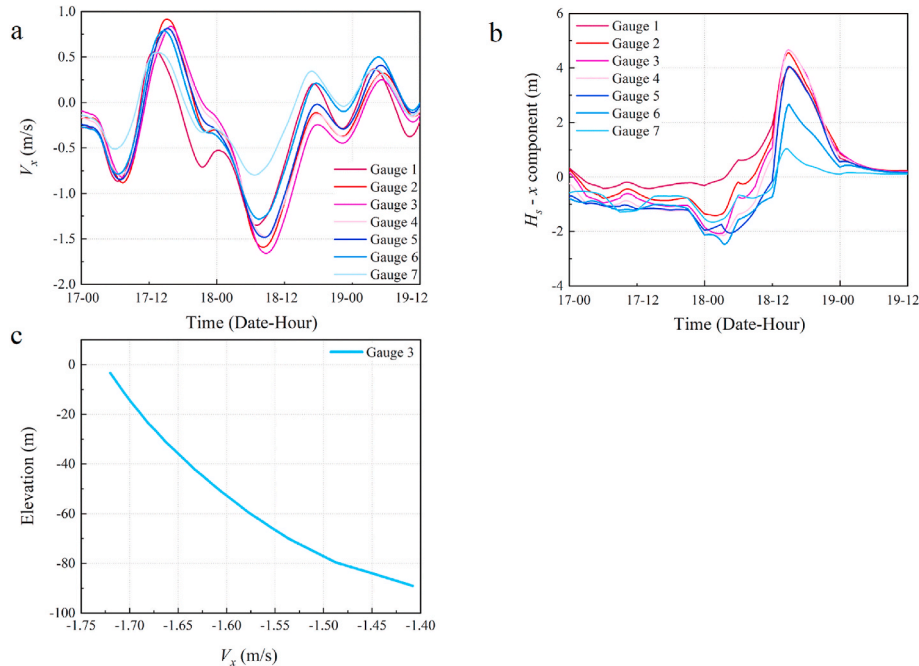

Fig. 13. Maximum water level (storm tide) in the Qiongzhou Strait.

occurred at 6:00–9:00 on July 18 at different virtual flow gauges along the optimal SFT heading; this is consistent with the time of the peak storm tide level (Fig. 10 (b)). However, unlike the tsunami, the maximum current acceleration of the typhoon storm surge is below 8×10^{-5} m/s^2, resulting in the drag force dominating the in-line forces of the SFT, with negligible inertia force. However, the vertical distribution of wind-driven flow is complex. In order to evaluate the SFT hydraulic forcing accurately, the current speed input to the inlet boundary of the CFD program should be carefully examined. Therefore, a three-

dimensional Delft3D-FLOW hydrodynamic model with 10 uniform vertical sigma layers, forced by the same conditions as the two-dimensional typhoon Rammasun model above, is adopted and compared. Fig. 14 (c) shows the current speed in x direction at 40 m below the surface (the SFT submergence depth) is around 1.64 m/s, which is nearly equal to the 1.65 m/s depth-averaged flow speed from the two-dimensional model. Hence, using the depth-averaged current speed is sufficient for SFT force analysis.

Fig. 15 shows the typhoon-induced wind velocity magnitude fields superimposed on wind speed vectors. The SFT cross section is affected by wave-induced orbital velocities normal to the tunnel tube, rather than the component parallel to the tunnel. To obtain the component of the wave-induced orbital velocity vector normal to the tube, the orbital velocity vector is multiplied by the sine of the angle between the velocity vector and the SFT heading. Since orbital velocities are proportional to the wave height, we determine the wave height using the corresponding x-component of the orbital velocities. The wave height at the seven virtual wave gauges on the optimal SFT heading is illustrated in Fig. 14 (b). At 10:00 on July 18, the typhoon eye entered the strait accompanied by low wind speed, resulting in low wave height in the Qiongzhou strait. As typhoon Rammasun moved north-westward at 14:00 on July 18, the wind speed in the strait dramatically increased. The maximum wind

Fig. 14. Storm tide in the Qiongzhou Strait. (a) Along-strait depth-averaged current speed at the seven virtual gauges. (b) Along-strait wave height at the seven virtual gauges. (c) Vertical distribution of current speed when gauge #3 reached its maximum current speed value. x direction: positive to east and negative to west.
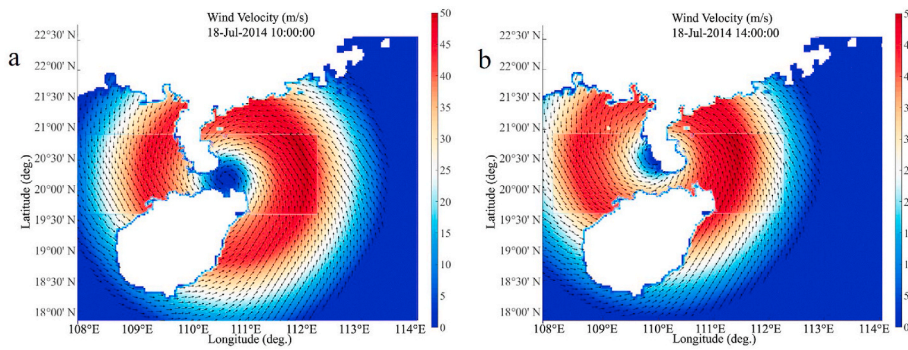
Fig. 15. Wind velocity field near the Qingzhou Strait. (a) wind velocity at 10:00 on July 18. (b) wind velocity at 14:00 on July 18.
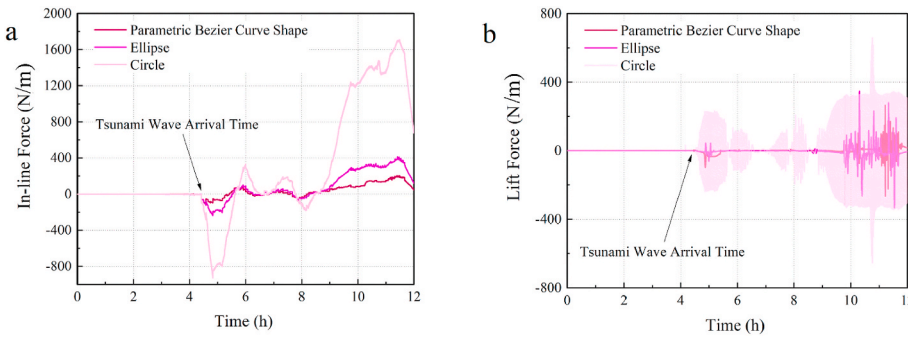

Fig. 16. Hydrodynamic forces on the SFT. (a) The in-line force on the SFT for different cross-sections. (b) The lift force on the SFT for different cross-sections.

speed at gauge #3 (110.164°E, 20.132°N) increased to around 30 m/s, and westerly wind dominated the strait, thus the wave height increased. The wave height reached its maximum value of 4.8 m, with a corresponding wave period of 5.08 s. The sheltering effect of Hainan Island reduces the wave height and wave period in the strait compared to the open sea. After the typhoon crossed over the strait, entered Beibu Gulf and made landfall in Guangxi Province, the wind intensity and wave height continuously decreased.

5.3. Tsunami impacts on the SFT

Fig. 16 (a) shows the temporal variation of in-line force (combined drag and inertial force) during the tsunami simulation with different SFT cross-sections. The maximum in-line force on all cross sectional shapes occurs at around 11.3 h, which is the same time as the peak inlet current speed (Fig. 12 (b)). For the parametric Bezier curve shape, the maximum in-line force is 200 N/m, which is half that of the elliptical SFT cross-section. However, the circular cross section shape experiences a maximum in-line force of 1700 N/m, which is over 8 times the force on the parametric Bezier curve cross section. In addition to this, the times of peak in-line force are not the same for all shapes. For the parametric Bezier curve shape, the first negative and positive maxima of inline force occur at around 4.5 h and 5.5 h, respectively, which are almost identical to the times of local peaks in acceleration (Fig. 12 (b)), indicating dominance of the inertia force. However, for the circular cross section, the first negative and positive maxima of inline force occur at around 4.8 h and 6.0 h, respectively, (Fig. 12 (b)), indicating dominance of the drag force. The elliptical cross section displays a phase between the other two shapes. Therefore, the in-line force on the elliptical SFT is a combined effect of inertial and drag forces.

Fig. 16 (b) shows the lift force during the tsunami simulation for different SFT cross-sections. The results indicate that severe vortex shedding occurs at about 11 h for the parametric Bezier curve shape, while it shows vortex shedding beginning before 10 h for the ellipse. The circular cross section experiences a larger lift force than the other shapes
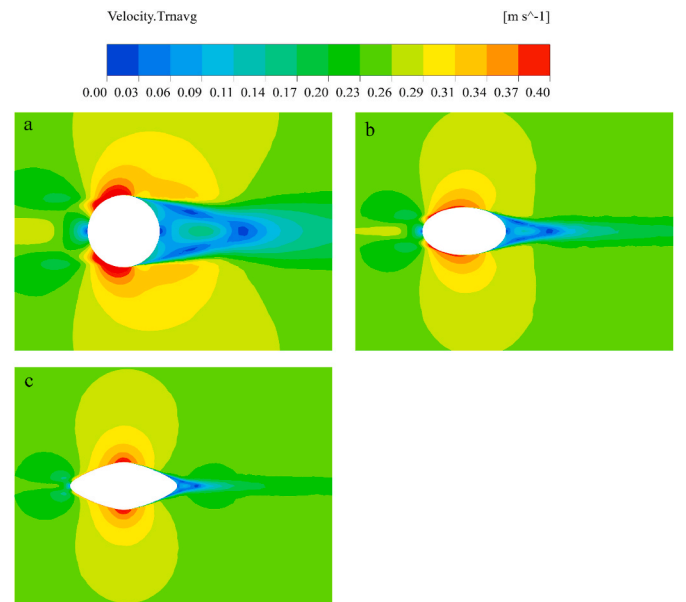

Fig. 17. Time-averaged velocity contours of different cross sectional shapes. (a) Circle. (b) Ellipse. (c) Parametric Bezier curve.

and vortex shedding begins just after the tsunami reaches the SFT heading in the Qiongzhou Strait. It should also be noted that the vortex shedding frequency of the circular SFT is higher than that of the other two SFT cross-sections.

Fig. 17 shows time-averaged velocity contours for the three different SFT cross-sections. The parametric Bezier curve profile (Fig. 17 (c)) is the most streamlined shape, with the furthest downstream separation point and the smallest wake region, thereby mitigating the in-line force on the SFT. This shape also experiences a maximum velocity lower than
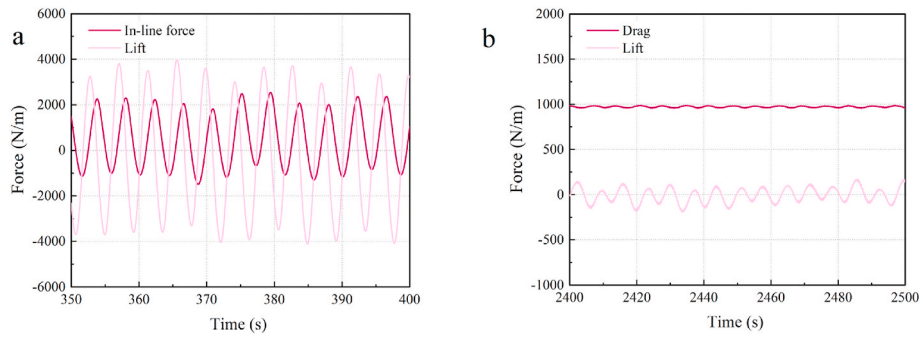
Fig. 18. Typhoon forces on the SFT in the Qiongzhou Strait. (a) Coupled wave-current model. (b) Steady current only model.

the other two cross-section shapes, resulting in a pressure more uniformly distributed along the SFT surface.

5.4. Typhoon impacts on the SFT

Section 5.3 shows that the parametric Bezier curve SFT cross-section has more favourable hydrodynamic performance than simpler shapes. Therefore, the parametric Bezier curve SFT cross-section is adopted for storm surge impact analysis. Fig. 18 (a) shows time series of in-line force and lift force on the SFT in the typhoon scenario. The maximum in-line force on the SFT is approximately 2500 N/m, whereas maximum lift is 4000 N/m. The in-line force and lift have the same fluctuation period of about 4.3 s, driven by the combined wave and current forcing at the inlet of the ANSYS Fluent simulation. The in-line force lags behind the lift with a phase difference, as expected for orbital flow induced by progressive surface waves.

Fig. 19 presents velocity contours around the SFT cross-section at $t = 400$ s. In the water phase, the velocity near the wave crest is high, whereas below the wave trough it is low. The velocity field is distorted near the SFT.

To better understand the differences of the wave and current impacts on the SFT, a simulation with only current (no wave) is conducted as a comparison. The mean current speed remains 1.65 m/s, the same as in the coupled wave-current model. The simulation ran for 2500 s, and time series of drag and lift during the final 100 s are shown in Fig. 18 (b). The maximum drag in this steady flow model is about 1000 N/m, half that of the wave-current case, indicating that waves and current

contribute equally to the in-line force. However, the lift in the current-only model is below 250 N/m, indicating the waves play a dominant role in lift. The large velocity fluctuation at the wave period disrupts the uniform pressure distribution on the upper and lower SFT surfaces, resulting in an apparent increase of lift. In the current-only case, the drag and lift both fluctuate with a small amplitude at a period of about 6.8 s, which is longer than the fluctuation period in the coupled wave-current case.

Since the wave height is determined using the corresponding *x*-component of the orbital velocities, the inline force of the SFT cross-section can be accurately calculated. However, the vertical force due to both the pressure fluctuation, and the vertical component of the orbital velocity is underestimated.

The maximum in-line force on the SFT in the typhoon case is 12.5 times larger than in the tsunami scenario, demonstrating that for an SFT in the Qiongzhou Strait, typhoon impacts are more destructive and challenging than tsunami. The SFT mooring system design and net buoyancy adjustment ability should take these hazards into account.

6. Conclusion

In this paper, we calculated the worst-case tsunami and hindcast typhoon impacts on hydrodynamic forcing on an SFT in the Qiongzhou Strait. In order to determine the optimal SFT cross-section under extreme events, we proposed a parametric Bezier curve SFT profile and compared the hydrodynamic response with other simpler cross-sections. The main conclusions are briefly summarized as follows:

(1) The Qiongzhou Strait is sheltered by Hainan Island, so is partially spared extreme event hazards. The tsunami arrival time at the optimal SFT heading is about 4.2 h after an earthquake in the Manilla Trench. The maximum current speed along the strait is 0.9 m/s. During the hindcast typhoon, however, maximum current speed along the strait is 1.65 m/s.

(2) Considering the in-line force components in the tsunami scenario, inertia plays an important role in the parametric Bezier curve shape, while for the circle shape, drag dominates the force. However, in the typhoon case, due to the slow variation of the mean current speed (from the storm surge, not from the waves, for which drag and inertia are both important), the inertial force can be neglected compared with the drag.

(3) The SFT cross-section using the parametric Bezier curve profile is recommended due to its streamlined shape and hydraulic force-mitigating effects. It experiences the minimum in-line force and the smallest wake region. Furthermore, serious vortex shedding is limited to a shorter time period and lower amplitude compared with other simpler shapes.

(4) In the typhoon scenario, the wave and current provide an approximately equal contribution to the in-line force. However, the waves play a dominant role in lift.
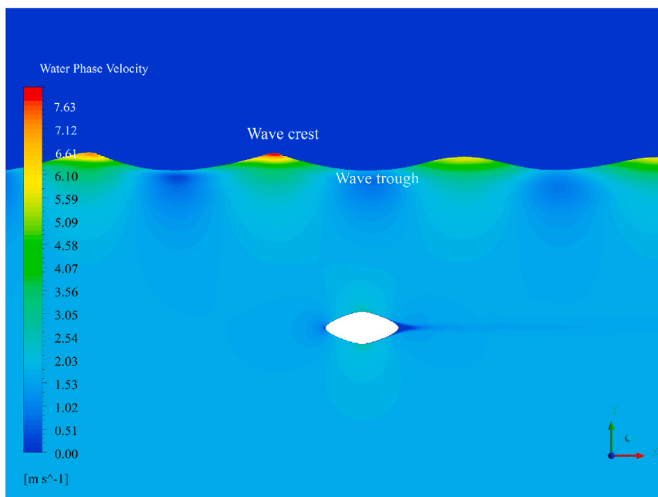

Fig. 19. Velocity contours around the SFT cross-section at $t = 400$ s. The upper dark blue region is air, and the lower region is water. (For interpretation of the references to colour in this figure legend, the reader is referred to the Web version of this article.)

(5) The typhoon is more devastating than the tsunami for an SFT in the Qiongzhou Strait. The maximum in-line force on the SFT in the typhoon case is 12.5 times higher than in the tsunami scenario. The necessity and importance of hazard assessment and structural vulnerability in typhoon scenarios should be emphasized throughout the processes of engineering design, construction, operation and maintenance of an SFT.

The present study investigated forces on an SFT cross-section under extreme events. Additional research is required to further analyze the SFT dynamic and structural response. The three-dimensional effects of the SFT will also be addressed in follow-on research.

CRediT authorship contribution statement

P.X. Zou: Methodology, Software, Validation, Visualization, Writing - original draft. **Jeremy D. Bricker:** Methodology, Software, Writing - review & editing, Supervision. **Wim S.J. Uijttewaal:** Writing - review & editing, Supervision.

Declaration of competing interest

The authors declare that they have no known competing financial interests or personal relationships that could have appeared to influence the work reported in this paper.

Acknowledgement

References

AASHTO, A., 2018. Policy on Geometric Design of Highways and Streets, seventh ed.
Bernard, E., Titov, V., 2015. Evolution of tsunami warning systems and products. Phil. Trans. Math. Phys. Eng. Sci. https://doi.org/10.1098/rsta.2014.0371.
biu Liu, K., Shen, C., sheun Louie, K., 2001. A 1,000-year history of typhoon landfalls in Guangdong, Southern China, reconstructed from Chinese historical documentary records. Ann. Assoc. Am. Geogr. https://doi.org/10.1111/0004-5608.00253.
Bricker, J.D., Nakayama, A., 2014. Contribution of trapped air, deck superelevation, and nearby structures to bridge deck failure during a tsunami. J. Hydraul. Eng. https://doi.org/10.1061/(ASCE)HY.1943-7900.0000855.
BRICKER, J.D., et al., 2014. Spatial variation of damage due to storm surge and waves during typhoon haiyan in the Philippines. J. Japan Soc. Civ. Eng. Ser. B2 (Coastal Eng. https://doi.org/10.2208/kaigan.70.I_231.
Caldwell, R.L., Edmonds, D.A., 2014. Delft3D-Flow: simulation of multi-dimensional hydrodynaminc flows and transport phenomena, including sediments-user manual. J. Geophys. Res. Earth Surf. https://doi.org/10.1002/2013JF002965.
Chen, J., Pan, X., Wang, C., Hu, G., Xu, H., Liu, P., 2019. Airfoil parameterization evaluation based on a modified PARASEC method for a H-Darrious rotor. Energy. https://doi.org/10.1016/j.energy.2019.115910.
Christie, R., Robinson, M., Tejero, F., MacManus, D.G., 2019. The use of hybrid intuitive class shape transformation curves in aerodynamic design. Aero. Sci. Technol. https://doi.org/10.1016/j.ast.2019.105473.
Coder, J.G., Maughmer, M.D., 2013. A CFD-compatible transition model using an amplification factor transport equation. https://doi.org/10.2514/6.2013-253.
Deng, S., Ren, H., Xu, Y., Fu, S., Moan, T., Gao, Z., 2020. Experimental study of vortex-induced vibration of a twin-tube submerged floating tunnel segment model. J. Fluid Struct. https://doi.org/10.1016/j.jfluidstructs.2020.102908.
Derksen, R.W., Rogalsky, T., 2010. Bezier-PARSEC: An optimized aerofoil parameterization for design. Adv. Eng. Software. https://doi.org/10.1016/j.advengsoft.2010.05.002.
Fenton, J.D., 1985. A fifth-order Stokes theory for steady waves. J. Waterw. Port, Coast. Ocean Eng. 111 (216), 2. https://doi.org/10.1061/(ASCE)0733-950X.
Gang, L., Xiao-jun, Z., Jian-xun, C., 2018. The dynamic response of an experimental floating tunnel with different cross sections under explosive impact. J. Coast. Res. https://doi.org/10.2112/si82-031.1.
Gross, J.M., DeMaria, M., Knaff, J.A., Sampson, C.R., 2004. A New Method for Determining Tropical Cyclone Wind Forecast Probabilities.
Haikou Meteorological Service, 2020. Haikou Meteorological Information Sharing Service System. http://www.hkqx.net/Science/specialTyphoon?id=44.
Hirt, C.W., Nichols, B.D., 1981. Volume of fluid (VOF) method for the dynamics of free boundaries. J. Comput. Phys. https://doi.org/10.1016/0021-9991(81)90145-5.
Holland, G.J., 1980. An analytic model of the wind and pressure profiles in hurricanes. Mon. Weather Rev. 2. https://doi.org/10.1175/1520-0493(1980)108<1212. AAMOTW>2.0.CO.
Holland, G., 2008. A revised hurricane pressure-wind model. Mon. Weather Rev. https://doi.org/10.1175/2008MWR2395.1.
Holland, G.J., Belanger, J.I., Fritz, A., 2010. A revised model for radial profiles of hurricane winds. Mon. Weather Rev. https://doi.org/10.1175/2010MWR3317.1.
Hong Nguyen, P., Cong Bui, Q., Ha Vu, P., The Pham, T., 2014. Scenario-based tsunami hazard assessment for the coast of Vietnam from the Manila Trench source. Phys. Earth Planet. In. https://doi.org/10.1016/j.pepi.2014.07.003.
il Seo, S., suk Mun, H., ho Lee, J., ha Kim, J., 2015. Simplified analysis for estimation of the behavior of a submerged floating tunnel in waves and experimental verification. Mar. Struct. https://doi.org/10.1016/j.marstruc.2015.09.002.
Imamura, F., Boret, S.P., Suppasri, A., Muhari, A., 2019. Recent occurrences of serious tsunami damage and the future challenges of tsunami disaster risk reduction. Prog. Disaster Sci. https://doi.org/10.1016/j.pdisas.2019.100009.
Jeong, U.Y., Koh, H.M., Lee, H.S., 2002. Finite element formulation for the analysis of turbulent wind flow passing bluff structures using the RNG k - ε model. J. Wind Eng. Ind. Aerod. https://doi.org/10.1016/S0167-6105(01)00190-8.
Jiang, B., Liang, B., Faggiano, B., Iovane, G., Mazzolani, F.M., 2018. Feasibility Study on a Submerged Floating Tunnel for the Qiongzhou Strait in China.
Jin, C., Kim, M.H., 2020. Tunnel-mooring-train coupled dynamic analysis for submerged floating tunnel under wave excitations. Appl. Ocean Res. https://doi.org/10.1016/j.apor.2019.102008.
Kharal, A., Saleem, A., 2012. Neural Networks Based Airfoil Generation for a Given Cp Using Bezier-PARSEC Parameterization. https://doi.org/10.1016/j.ast.2011.08.010.
Kristoffersen, M., Minoretti, A., Børvik, T., 2019. On the internal blast loading of submerged floating tunnels in concrete with circular and rectangular cross-sections. Eng. Fail. Anal. https://doi.org/10.1016/j.engfailanal.2019.04.074.
Kunisu, H., 2010. Evaluation of Wave Force Acting on Submerged Floating Tunnels. https://doi.org/10.1016/j.proeng.2010.08.012.
Langtry, R.B., Menter, F.R., 2009. Correlation-based transition modeling for unstructured parallelized computational fluid dynamics codes. AIAA J. https://doi.org/10.2514/1.42362.
Li, K., Jiang, X., 2016. Research on Section Form of Submerged Floating Tunnels Considering Structural Internal Force Optimization under Fluid Action. https://doi.org/10.1016/j.proeng.2016.11.551.
Li, X., Zhang, W., 2019. 3D numerical simulation of wave transmission for low-crested and submerged breakwaters. Coast. Eng. https://doi.org/10.1016/j.coastaleng.2019.103517.
Lin, H., Xiang, Y., Yang, Y., 2019. Vehicle-tunnel coupled vibration analysis of submerged floating tunnel due to tether parametric excitation. Mar. Struct. https://doi.org/10.1016/j.marstruc.2019.102646.
Liu, P.L.F., Wang, X., Salisbury, A.J., 2009. Tsunami hazard and early warning system in South China Sea. J. Asian Earth Sci. https://doi.org/10.1016/j.jseaes.2008.12.010.
Mandara, A., Russo, E., Faggiano, B., Mazzolani, F.M., 2016. Analysis of Fluid-Structure Interaction for a Submerged Floating Tunnel. https://doi.org/10.1016/j.proeng.2016.11.572.
Megawati, K., et al., 2009. Tsunami hazard from the subduction megathrust of the South China Sea: Part I. Source characterization and the resulting tsunami. J. Asian Earth Sci. https://doi.org/10.1016/j.jseaes.2008.11.012.
Michel, G.W., Becker, M., Reigber, C., Tibi, R., Yu, Y.Q., Zhu, S.Y., 2001. Regional GPS data confirm high strain accumulation prior to the 2000 June 4 Mw = 7.8 earthquake at Southeast Sumatra. Geophys. J. Int. https://doi.org/10.1046/j.0956-540X.2001.01469.x.
Muhammad, N., Ullah, Z., Choi, D.H., 2017. Performance evaluation of submerged floating tunnel subjected to hydrodynamic and seismic excitations. Appl. Sci. https://doi.org/10.3390/app7111122.
GEBCO: General Bathymetric Chart of the Oceans. https://www.gebco.net, 2020.
Okada, Y., 1992. Internal deformation due to shear and tensile faults in a half-space. Bull. Seismol. Soc. Am. 82 (2), 1018–1040.
OSU TPXO Tide Model, 2020. https://www.tpxo.net/global.
Pawar, S., Brizzolara, S., 2019. Relevance of transition turbulent model for hydrodynamic characteristics of low Reynolds number propeller. Appl. Ocean Res. https://doi.org/10.1016/j.apor.2019.02.018.
Ren, Z.Y., Zhao, X., long Wang, B., Dias, F., Liu, H., 2017. Characteristics of wave amplitude and currents in South China Sea induced by a virtual extreme tsunami. J. Hydrodyn. https://doi.org/10.1016/S1001-6058(16)60747-3.
Roeber, V., Bricker, J.D., 2015. Destructive tsunami-like wave generated by surf beat over a coral reef during Typhoon Haiyan. Nat. Commun. https://doi.org/10.1038/ncomms8854.
CMA Tropical Cyclone Data Center.TC size analysis. (tcdata.typhoon.org.cn).
Shengzhong, W., Xiang, C., Qinxi, L., Gengren, C., 2016. Research on Type Selection of Submerged Floating Tunnel of Qiongzhou Strait. https://doi.org/10.1016/j.proeng.2016.11.553.
Shi, X., Liu, S., Yang, S., Liu, Q., Tan, J., Guo, Z., 2015. "Spatial–temporal distribution of storm surge damage in the coastal areas of China. Nat. Hazards. https://doi.org/10.1007/s11069-015-1838-z.
Tian, W., Song, B., Ding, H., 2019. Numerical research on the influence of surface waves on the hydrodynamic performance of an AUV. Ocean Eng. https://doi.org/10.1016/j.oceaneng.2019.04.007.
Wang, Y., Gao, T., Han, Z., Liu, Q., 2017. "Impacts of wind-field correction on the numerical simulation of storm-surge inundation during typhoon 'Rammasun. Estuar. Coast Shelf Sci. https://doi.org/10.1016/j.ecss.2017.07.006.

Wankang, Y., Baoshu, Y., Xingru, F., Dezhou, Y., Guandong, G., Haiying, C., 2019. The effect of nonlinear factors on tide-surge interaction: a case study of Typhoon Rammasun in Tieshan Bay, China. Estuar. Coast Shelf Sci. https://doi.org/10.1016/j.ecss.2019.01.024.

Wauters, J., Degroote, J., 2018. On the study of transitional low-Reynolds number flows over airfoils operating at high angles of attack and their prediction using transitional turbulence models. Prog. Aero. Sci. https://doi.org/10.1016/j.paerosci.2018.10.004.

Wu, T.R., Huang, H.C., 2009. Modeling tsunami hazards from Manila trench to Taiwan. J. Asian Earth Sci. https://doi.org/10.1016/j.jseaes.2008.12.006.

Xu, J., Fu, Z., Bai, J., Zhang, Y., Duan, Z., Zhang, Y., 2018. Study of boundary layer transition on supercritical natural laminar flow wing at high Reynolds number through wind tunnel experiment. Aero. Sci. Technol. https://doi.org/10.1016/j.ast.2018.07.007.

Yan, H., Zhang, F., Yu, J., 2016. The Lectotype Optimization Study on Submerged Floating Tunnel Based Delphi Method. https://doi.org/10.1016/j.proeng.2016.11.574.

Yin, K., Xu, S., Zhao, Q., Huang, W., Yang, K., Guo, M., 2020. Effects of land cover change on atmospheric and storm surge modeling during typhoon event. Ocean Eng. https://doi.org/10.1016/j.oceaneng.2020.106971.

Zhang, K., Xiang, Y., Du, Y., 2010. Research on Tubular Segment Design of Submerged Floating Tunnel. https://doi.org/10.1016/j.proeng.2010.08.023.

Zhao, X., Jiang, Y., Ren, Z., Liu, H., 2017. Historical tsunami records and potential tsunami scenarios near Haikou coastal region. Nat. Hazards. https://doi.org/10.1007/s11069-017-2983-3.

Zou, P., Bricker, J., Uijttewaal, W., 2020. Optimization of submerged floating tunnel cross section based on parametric Bézier curves and hybrid backpropagation - genetic algorithm. Mar. Struct. https://doi.org/10.1016/j.marstruc.2020.102807.